A combined finite element and spectral procedure for radio-frequency sheath-plasma interactions

Haruhiko Kohno[a,*], James R. Myra[b], Daniel A. D'Ippolito[b]

[a] *Department of Physics, Lehigh University, 16 Memorial Drive East, Bethlehem, PA 18015, USA*

[b] *Lodestar Research Corporation, 2400 Central Avenue P-5, Boulder, CO 80301, USA*

Abstract

A combined finite element and spectral scheme is presented for analyzing self-consistent radio-frequency (RF) sheath-plasma interactions in the ion cyclotron range of frequencies. The present method provides a stable solution even for the case where grids are not fine enough to resolve the exponential decay length of the wave mode along the sheath. The key feature in the method is that a spectral discretization is applied to the boundary condition equation that models RF sheath-plasma interactions and this is combined with a finite element discretization of the volume equation that governs cold plasma behavior. Several two-dimensional problems including linear and nonlinear cases are given to illustrate the capabilities of the present approach.

Keywords: Finite element methods, Spectral methods, Plasma waves, Radio-frequency sheaths, Cold plasma, Magnetic confinement fusion

1. Introduction

In the quest for the production of fusion energy from tokamaks [1, 2] or other magnetically confined plasmas, some form of plasma heating and

*Corresponding author. The present affiliation of the corresponding author is as follows: Department of Mechanical Information Science and Technology, Kyushu Institute of Technology, 680-4 Kawazu, Iizuka, Fukuoka 820-8502, Japan.

Email addresses: kohno@mse.kyutech.ac.jp (Haruhiko Kohno), jrmyra@lodestar.com (James R. Myra), dippolito@lodestar.com (Daniel A. D'Ippolito)

control is generally required. The application of radio-frequency (RF) waves in the ion cyclotron range of frequencies (ICRF) is one such heating method [3], which can also be used to influence other plasma properties such as currents and flows. While much success has been achieved with ICRF, in some operational regimes strong deleterious interactions with the walls and limiters of the device are observed in the scrape-off layer (SOL) [4–8]. A desire to better model these plasma-ICRF-surface interactions is the motivation for the present work.

While identifying and modeling all the possible active mechanisms at work is still an active subject of research, ICRF driven sheaths are thought to be an important mechanism which we take as the basis for the numerical model presented here, i.e., the rfSOL (RF sheath-plasma interactions in the SOL) code. The physics of ICRF sheaths has been reviewed in [9, 10] and initial applications of the numerical model embedded in the rfSOL code [11] were discussed in Ref. [12]. Briefly, the model describes standard RF plasma wave propagation in the interior volume region using a cold plasma dielectric function. These waves then interact with a wall sheath which is described by a sheath boundary condition (sheath BC) [13, 14] on the surface of the interior region (or some subset of the surface).

The model described by Maxwell's equations combined with the sheath BC at the boundary turns out to give rise to a number of new phenomena which are both physically interesting and numerically challenging. In particular, the wave interaction with the sheath is sensitive to details of the device geometry and magnetic field configurations, which motivates the use of finite element methods. It has been observed in the present model that short-scale length modes can appear on the sheath surface depending on the contact angle between the magnetic field line and the wall, plasma density, and wave-field patterns. After thorough numerical investigation, it has been found that some of the observed fine-scale variations have no physical meaning, but are caused by numerical instability under certain conditions. Specifically, in order to avoid unwanted numerical oscillation, sufficient spatial resolution is required in the perpendicular direction to the sheath surface when the contact angle between the magnetic field line and the wall becomes very small and thereby the decay length of the wave mode, in particular, the sheath-plasma wave (SPW), becomes considerably smaller than that for a larger contact angle (as will be shown in Figure 5 later). If the numerically induced modes occur in a size comparable to or smaller than calculation grid lengths on the sheath, unstable grid-scale oscillation can be generated and

propagate along the sheath; in some cases this numerical error becomes so significant that it can spoil a numerical solution over a wide range. On the other hand, if the numerical instability occurs in unimportant regions, for example, where the contribution of the RF sheath is sufficiently small, a numerical scheme that bypasses the requirement of high resolution near the sheath is desirable.

The objective in this paper is to present a combined finite element and spectral approach which can stably solve any RF sheath-plasma interaction problems in the ICRF. The spectral method is well known to yield accurate solutions when solution profiles are sufficiently smooth [15–17], and there have been several papers which demonstrate combined techniques of finite element and spectral methods for different purposes [18–22]. In our approach, a spectral method is applied to the discretization of the sheath BC to assure stability of solutions. The basic concept is that unstable grid-scale oscillations generated on the sheath surface as a consequence of imposing the sheath BC under insufficient grid resolution can be avoided by introducing a finite cutoff number of harmonics in the spectral discretization. This approach prevents the grid-scale oscillations from propagating from regions where errors are particularly generated. Since the finite element method is still applied to the plasma volume, the resultant global matrix is mostly sparse, which makes it possible to compute a global matrix equation with modest computational effort by employing an appropriate sparse matrix solver.

The present paper is organized as follows. In Section 2, we briefly review the model for the numerical analysis of RF sheath-plasma interactions. The combined finite element and spectral approach is then presented in detail for both linear and nonlinear cases in Section 3. The validity of the developed scheme is tested by comparing the numerical results with those obtained by the previous finite element approach under the same conditions, and a challenging example which triggers unstable modes on the sheath surface is solved by the new numerical method in Section 4. Finally, conclusions of the present work are offered in Section 5.

2. Problem formulation for RF sheath-plasma interactions

In this section, we briefly summarize the equations that govern the behavior of plasma waves in the SOL and the interaction between the waves and the sheaths on metal surfaces in the ICRF.

The governing equation for plasma waves in the SOL is a combined form of Maxwell's equations described as

$$\nabla \times \nabla \times \boldsymbol{E} - \frac{\omega^2}{c^2}\boldsymbol{\epsilon} \cdot \boldsymbol{E} - \mathrm{i}\omega\mu_0 \boldsymbol{J}_{\mathrm{ext}} = \boldsymbol{0}, \tag{1}$$

where the electric field $\boldsymbol{E}$ and the external current $\boldsymbol{J}_{\mathrm{ext}}$ vary on the RF time scale (i.e., $\boldsymbol{E}$, $\boldsymbol{J}_{\mathrm{ext}} \propto \mathrm{e}^{-\mathrm{i}\omega t}$). Here, ω is the applied ICRF wave frequency, c is the speed of light, having a relation with the dielectric constant ε_0 and the permeability μ_0 in vacuum, which is expressed as $c^2 = (\varepsilon_0\mu_0)^{-1}$, and i is the imaginary unit. The dielectric tensor $\boldsymbol{\epsilon}$ is given by

$$\boldsymbol{\epsilon} = (\boldsymbol{I} - \boldsymbol{bb})\,\varepsilon_\perp + \boldsymbol{bb}\varepsilon_\parallel + \mathrm{i}\boldsymbol{b} \times \boldsymbol{I}\varepsilon_\times, \tag{2}$$

where $\boldsymbol{I}$ is the unit tensor, and $\boldsymbol{b}$ is the unit vector along the background magnetic field $\boldsymbol{B}_0$ ($\boldsymbol{b} = \boldsymbol{B}_0/\left|\boldsymbol{B}_0\right|$); the subscript 0 denotes an equilibrium quantity. Here, the coefficients $\varepsilon_\perp$, $\varepsilon_\parallel$, and $\varepsilon_\times$ are expressed as follows:

$$\varepsilon_\perp = 1 - \sum_j \frac{\omega_{\mathrm{p}j}^2}{\omega^2 - \Omega_j^2}, \quad \varepsilon_\parallel = 1 - \sum_j \frac{\omega_{\mathrm{p}j}^2}{\omega^2}, \quad \varepsilon_\times = \sum_j \frac{\omega_{\mathrm{p}j}^2 \Omega_j}{\omega\left(\omega^2 - \Omega_j^2\right)}, \tag{3}$$

where $\omega_{\mathrm{p}j}$ and Ω_j are the plasma frequency and gyro frequency defined as $\omega_{\mathrm{p}j} = \left(n_{j0}e^2/\varepsilon_0 m_j\right)^{1/2}$ and $\Omega_j = q_j B_0/m_j$, respectively; the subscript j indicates two-species particles, i.e., an ion (i) or an electron (e), n_{j0} is the plasma number density, e and q_j are the electric charge ($|q_j| = e$), m_j is the ion or electron mass, and $B_0 = |\boldsymbol{B}_0|$. Throughout this study, we assume that quasi-neutrality in the plasma is retained, i.e., $n_{\mathrm{e}0} = n_{\mathrm{i}0} = n_0$.

At the metal wall, the RF sheath effect is taken into account by means of the sheath BC, which is written as follows:

$$\boldsymbol{E}_\tau = \nabla_\tau \left(\frac{\Delta_{\mathrm{sh}}}{\varepsilon_{\mathrm{sh}}} D_{\mathrm{n}} \right). \tag{4}$$

Here, Δ_{sh} is the time-averaged sheath width, $\varepsilon_{\mathrm{sh}}$ is the dielectric constant in the sheath (in this study we assume that $\varepsilon_{\mathrm{sh}} = \varepsilon_0$), D_{n} ($= \varepsilon_0 \boldsymbol{s} \cdot \boldsymbol{\epsilon} \cdot \boldsymbol{E}$) is the component of the electric displacement normal to the sheath (and $\boldsymbol{s}$ in the definition is the unit vector normal to the sheath pointing into the plasma), and the subscript τ denotes the two components tangential to the boundary. The right-hand side of Eq. (4) contains the physics of

sheath capacitance. The sheath BC reduces to the conducting-wall boundary condition (conducting-wall BC) for $\Delta_{\mathrm{sh}} \to 0$. In a manner consistent with the Child-Langmuir law [23, 24], the sheath width is written as follows:

$$\Delta_{\mathrm{sh}} = \left(\frac{eC_{\mathrm{sh}}}{\varepsilon_{\mathrm{sh}} T_{\mathrm{e}}} \left| D_{\mathrm{n}} \right| \right)^3 \lambda_{\mathrm{De}}^4 + C_{\mathrm{th}} \lambda_{\mathrm{De}}, \tag{5}$$

where C_{sh} is an order-unity constant (which is fixed at 0.6 in this study), T_{e} is the electron temperature, λ_{De} is the electron Debye length defined as $\lambda_{\mathrm{De}} = \left(\varepsilon_0 T_{\mathrm{e}} / n_{\mathrm{e}0} e^2 \right)^{1/2}$. The coefficient C_{th} is given by

$$C_{\mathrm{th}} = \begin{cases} 0 & \text{for } \sin\vartheta \leq \left(m_{\mathrm{e}} / m_{\mathrm{i}} \right)^{1/2} \\ \left\{ \ln \left[\left(\frac{m_{\mathrm{i}}}{m_{\mathrm{e}}} \right)^{1/2} \sin\vartheta \right] \right\}^{3/4} & \text{for } \sin\vartheta > \left(m_{\mathrm{e}} / m_{\mathrm{i}} \right)^{1/2}, \end{cases} \tag{6}$$

where ϑ is the angle between the magnetic field line (based on the background magnetic field, $\boldsymbol{B}_0$) and the sheath surface, defined such that $\sin\vartheta = \left| B_{0\mathrm{n}} \right| / \left| \boldsymbol{B}_0 \right|$ where $B_{0\mathrm{n}}$ is the perpendicular component of the background magnetic field to the wall. The first and second terms in Eq. (5) are the RF and thermal sheath contributions to the self-consistent sheath width, respectively. Sheath models similar to the capacitive sheath model employed here have also been derived in the plasma processing literature [25, 26].

3. Discretization of the governing equations

In our previous work [11], the sheath BC was discretized using a one-dimensional (1D) finite element method. In this study, we aim at discretizing the sheath BC using a spectral method and construct a system of algebraic equations in conjunction with the finite element discretization of the governing equation for the plasma volume. We first review the discretized equations in the plasma volume in Section 3.1, and then from Section 3.2 focus on the discretization of the sheath BC. Note that the dielectric tensor, the sheath BC, and Maxwell's equations are defined in three-dimensional (3D) space, and the latter also in time. The assumption of Fourier modes in z and t allows these dependencies to be taken into account analytically, hence the discretized equations will turn out to be independent of z and t.

3.1. Discretization of Maxwell's equation

As in our previous approach, the combined form of Maxwell's equations, Eq. (1), is discretized in the x-y plane by a two-dimensional (2D) finite element method. The weak form of Maxwell's equation for the plasma volume is given by

$$\int_{\Omega} \left(\nabla \times \boldsymbol{W} \cdot \nabla \times \boldsymbol{E} - \frac{\omega^2}{c^2} \boldsymbol{W} \cdot \boldsymbol{\epsilon} \cdot \boldsymbol{E} - \mathrm{i}\omega\mu_0 \boldsymbol{W} \cdot \boldsymbol{J}_{\mathrm{ext}} \right) \mathrm{d}\Omega = 0, \tag{7}$$

where Ω represents the calculation domain, and $\boldsymbol{W}$ is the weight function. Here, the weight function is chosen such that its tangential components are zero ($\boldsymbol{W}_\tau = \boldsymbol{0}$) on the boundary, since the sheath BC or the absorbing boundary condition (absorbing BC), which will be defined later, is imposed as a boundary condition; therefore, the boundary integral term is omitted in the derivation of Eq. (7) (see Ref. [11] for details).

Although Eq. (1) corresponds to the 3D representation of the physical quantities including the weight function, we assume a Fourier mode in the z components of $\boldsymbol{E}$, $\boldsymbol{J}_{\mathrm{ext}}$, and $\boldsymbol{W}$ in the Cartesian coordinate system. This is what permits the governing equation to be spatially discretized in the x-y plane in this analysis. The calculation domain is divided into nine-node quadrilateral grid elements, and then the weight function and electric field are defined based on the standard Galerkin approach as follows:

$$\boldsymbol{W} = \hat{\boldsymbol{W}}_i N_i(x, y)\, \mathrm{e}^{-\mathrm{i}k_z z} = \tilde{N}_i \hat{\boldsymbol{W}}_i, \tag{8}$$

$$\boldsymbol{E} = \hat{\boldsymbol{E}}_j N_j(x, y)\, \mathrm{e}^{\mathrm{i}(k_z z - \omega t)} = \tilde{N}_j \hat{\boldsymbol{E}}_j \mathrm{e}^{-\mathrm{i}\omega t}, \tag{9}$$

where N_i and N_j are the piecewise biquadratic interpolation functions, k_z is the wavenumber component in the z direction, $\hat{\boldsymbol{W}}_i$ and $\hat{\boldsymbol{E}}_j$ are the nodal vectors, and the subscripts i and j denote the global node number. The summation convention applies to the subscripts i and j. We note that readers should not confuse the subscript i with the imaginary unit i. The former is always used as a subscript and is italicized.

Substituting Eqs. (8) and (9) into Eq. (7) and then due to the requirement that the equation needs to be satisfied for arbitrary $\hat{\boldsymbol{W}}_i$, the algebraic equations for the plasma volume are derived as follows:

$$\boldsymbol{F} = \boldsymbol{R}, \tag{10}$$

where

$$\boldsymbol{F} = \int_{\Omega} \left[\nabla \times \left(\tilde{N}_j \hat{\boldsymbol{E}}_j \right) \times \nabla \tilde{N}_i - \frac{\omega^2}{c^2} N_i N_j N_k \boldsymbol{\epsilon}_k \cdot \hat{\boldsymbol{E}}_j \right] \mathrm{d}\Omega, \tag{11}$$

$$\boldsymbol{R} = \mathrm{i}\omega\mu_0 \int_{\Omega} N_i \boldsymbol{J}_{\mathrm{ant}} \mathrm{d}\Omega. \tag{12}$$

Here, the dielectric tensor is interpolated as $\boldsymbol{\epsilon} = N_k \boldsymbol{\epsilon}_k$ using its nodal values $\boldsymbol{\epsilon}_k$, and the external current is expressed as

$$\boldsymbol{J}_{\mathrm{ext}} = \boldsymbol{J}_{\mathrm{ant}} \mathrm{e}^{\mathrm{i}(k_z z - \omega t)}. \tag{13}$$

Note that the exponential functions that include z and t are cancelled out and not included in Eq. (10). On the boundary Γ where we impose the condition $\boldsymbol{W}_\tau = \boldsymbol{0}$, the algebraic equations are given by

$$\boldsymbol{s}_i \cdot \boldsymbol{F} = 0, \tag{14}$$

where $\boldsymbol{s}_i$ is the unit normal vector at the node i to the boundary Γ. In Eq. (14), we note that the summation convention is not applied to the subscript i.

3.2. Discretization of the sheath BC

For both linear and nonlinear cases, the sheath BC described in Eq. (4) is discretized based on the weighted residual method as it is for a finite element method. Forming the inner product of Eq. (4) with the weight function $\boldsymbol{W}^{\mathrm{S}}$, and then integrating it over the sheath region Γ^{S} yields

$$\int_{\Gamma^{\mathrm{S}}} \boldsymbol{W}^{\mathrm{S}} \cdot \left[\boldsymbol{E}_\tau - \nabla_\tau \left(\Delta_{\mathrm{sh}} \kappa \right) \right] \mathrm{d}\Gamma^{\mathrm{S}} = 0, \tag{15}$$

where $\kappa = \boldsymbol{s} \cdot \boldsymbol{\epsilon} \cdot \boldsymbol{E}$. Hereafter, the superscript S is occasionally attached to the quantities which are positioned on Γ^{S} for clarity. For simplicity, we assume that the sheath is formed on a flat wall that lies in the y-z plane as shown in Fig. 1. Thus, the normal direction to the sheath is $\boldsymbol{s} = \pm \boldsymbol{e}_x$ where $\boldsymbol{e}_x$ is the unit vector in the x direction, and the tangential directions, τ, correspond to $\boldsymbol{e}_y$ and $\boldsymbol{e}_z$ which are the unit vectors in the y and z directions, respectively. For the spectral discretization, the weight function and electric

field are defined as

$$\boldsymbol{W}^{\mathrm{S}} = \sum_{l=-N_{\mathrm{F}}}^{N_{\mathrm{F}}} \hat{\boldsymbol{W}}_l^{\mathrm{S}} \mathrm{e}^{-\mathrm{i}(lk_{\mathrm{s}}y+k_z z)}, \tag{16}$$

$$\boldsymbol{E}_\tau = \sum_{m=-N_{\mathrm{F}}}^{N_{\mathrm{F}}} \hat{\boldsymbol{E}}_{\tau m}^{\mathrm{S}} \mathrm{e}^{\mathrm{i}(mk_{\mathrm{s}}y+k_z z-\omega t)}, \tag{17}$$

where N_{F} is the cutoff number of harmonics, $\hat{\boldsymbol{W}}_l^{\mathrm{S}}$ and $\hat{\boldsymbol{E}}_{\tau m}^{\mathrm{S}}$ are constant vector coefficients, and $k_{\mathrm{s}} = 2\pi/L_y$; L_y is the length of the flat wall to which periodicity is applied in the y direction. Notice that the spectral discretization is applied only to the electric field components tangential to the sheath surface; the electric field component normal to the sheath surface is discretized according to Eq. (9). Considering that Eq. (15) needs to be satisfied for arbitrary $\hat{\boldsymbol{W}}_l^{\mathrm{S}}$, one gets

$$\int_{\Gamma^{\mathrm{S}}} \mathrm{e}^{-\mathrm{i}(lk_{\mathrm{s}}y+k_z z)} \left[\boldsymbol{E}_\tau - \nabla_\tau \left(\Delta_{\mathrm{sh}}\kappa\right)\right] \mathrm{d}\Gamma^{\mathrm{S}} = \boldsymbol{0}. \tag{18}$$

Note that this holds for different l. In the following sub-subsections, we first show the spectral discretization procedure for the linear sheath BC and then advance the procedure to solve the nonlinear sheath-plasma interactions. For clarity, the numerical solution in this approach consists of (1) the nodal values of the electric field in the plasma volume and the normal component of the electric field at the boundary for finite element discretization (see Eq. (9)) and (2) the coefficients of Fourier series of the electric field components tangential to the sheath surface for spectral discretization (see Eq. (17)).

3.2.1. Linear sheath BC

At the left boundary where $\boldsymbol{s} = \boldsymbol{e}_x$, the y component of the integral equation (18) is written as

$$\int_{\Gamma^{\mathrm{S}}} \mathrm{e}^{-\mathrm{i}(lk_{\mathrm{s}}y+k_z z)} \left[E_y - \boldsymbol{e}_x \cdot \frac{\partial}{\partial y}\left(\Delta_{\mathrm{sh}}\boldsymbol{\epsilon} \cdot \boldsymbol{E}\right)\right] \mathrm{d}\Gamma^{\mathrm{S}} = 0. \tag{19}$$

First, let us consider the linear case where the first term on the right-hand side of Eq. (5) is omitted as being negligibly small. When we approximate the product of Δ_{sh} and $\boldsymbol{\epsilon}$, which is defined as $\boldsymbol{\chi}$, using the following Fourier

series

$$\boldsymbol{\chi} = \Delta_{\mathrm{sh}}\boldsymbol{\epsilon} \simeq \sum_{n=-N_{\mathrm{F}}}^{N_{\mathrm{F}}} \boldsymbol{\chi}_n^{\mathrm{S}} \mathrm{e}^{\mathrm{i}nk_{\mathrm{s}}y}, \tag{20}$$

where

$$\boldsymbol{\chi}_n^{\mathrm{S}} = \frac{1}{L_y}\int_0^{L_y} \boldsymbol{\chi}\mathrm{e}^{-\mathrm{i}nk_{\mathrm{s}}y}\mathrm{d}y, \tag{21}$$

we obtain

$$\begin{aligned} &\hat{E}_{yl}^{\mathrm{S}} - \sum_{m=\max(-N_{\mathrm{F}},-N_{\mathrm{F}}+l)}^{\min(N_{\mathrm{F}},N_{\mathrm{F}}+l)} \mathrm{i}lk_{\mathrm{s}} \\ &\cdot \left(\chi_{xx(l-m)}^{\mathrm{S}}\hat{E}_{xm}^{\mathrm{S}} + \chi_{xy(l-m)}^{\mathrm{S}}\hat{E}_{ym}^{\mathrm{S}} + \chi_{xz(l-m)}^{\mathrm{S}}\hat{E}_{zm}^{\mathrm{S}}\right) = 0 \end{aligned} \tag{22}$$

after substituting Eqs. (17) and (20) into Eq. (19). Notice that Eq. (22) does not include z and t. Also, note that $\hat{E}_{xm}^{\mathrm{S}}$ in Eq. (22) are not independent variables since only the components of $\boldsymbol{E}$ tangential to the sheath surface (in this case, E_y and E_z) are expressed as their Fourier series in y as shown in Eq. (17). In fact, the component of $\boldsymbol{E}$ normal to the sheath surface is a part of the finite element solution and defined at each grid node on the boundary. Therefore, the relation between the nodal values of E_x and $\hat{E}_{xm}^{\mathrm{S}}$ is given by

$$N_j^{\mathrm{S}}(y)\,\hat{E}_{xj}^{(\mathrm{F})} \simeq \sum_{m=-N_{\mathrm{F}}}^{N_{\mathrm{F}}} \hat{E}_{xm}^{\mathrm{S}}\mathrm{e}^{\mathrm{i}mk_{\mathrm{s}}y}, \tag{23}$$

where N_j^{S} are the piecewise quadratic interpolation functions corresponding to Eq. (9) and the subscript j denotes the global node number on Γ^{S}. Here the summation convention applies to the subscript j, and the superscript F is attached in $\hat{E}_{xj}^{(\mathrm{F})}$ to explicitly show that the variable is originated from the finite element discretization applied to the plasma volume. The expression for $\hat{E}_{xm}^{\mathrm{S}}$ used in Eq. (22) is then obtained as

$$\hat{E}_{xm}^{\mathrm{S}} = \bar{N}_{m,j}^{\mathrm{S}}\hat{E}_{xj}^{(\mathrm{F})}, \tag{24}$$

where

$$\bar{N}_{m,j}^{\mathrm{S}} \equiv \frac{1}{L_y}\int_0^{L_y} N_j^{\mathrm{S}}\mathrm{e}^{-\mathrm{i}mk_{\mathrm{s}}y}\mathrm{d}y. \tag{25}$$

The integral in Eq. (25) can be analytically calculated (see Appendix A).

The z component of the integral equation (18) is discretized in a similar way, and the result is mostly the same as Eq. (22), except that $\hat{E}^{\mathrm{S}}_{yl} \to \hat{E}^{\mathrm{S}}_{zl}$ and $lk_{\mathrm{s}} \to k_z$. Also, the discretized expressions at the right boundary are obtained simply by replacing with $\boldsymbol{s} = -\boldsymbol{e}_x$. The system of algebraic equations for the entire system consists of Eqs. (10), (14), and (22) together with the contributions of the above-mentioned z component of the sheath BC and the sheath BC at the right wall.

Since the Fourier coefficients $\hat{\boldsymbol{E}}^{\mathrm{S}}_{\tau m}$ do not correspond to the nodal values at the sheath surface, the following conversion is necessary for the finite element discretization at the boundary:

$$\hat{\boldsymbol{E}}^{(\mathrm{F})}_{\tau j}\Big|_{\mathrm{boundary}} = \sum_{m=-N_{\mathrm{F}}}^{N_{\mathrm{F}}} \hat{\boldsymbol{E}}^{\mathrm{S}}_{\tau m} \mathrm{e}^{\mathrm{i}mk_{\mathrm{s}}y_j}, \tag{26}$$

where the subscript j denotes the boundary node and y_j is its coordinate value in y.

3.2.2. Nonlinear sheath BC

As a next step, we take into account the nonlinear term in the expression for the sheath width (see Eq. (5)). Again, let us consider the y component of the integral equation (18) at the left boundary as an example. Substituting Eqs. (5) and (17) into Eq. (19) yields

$$\begin{aligned} &\hat{E}^{\mathrm{S}}_{yl} L_y - \int_{\Gamma^{\mathrm{S}}} \alpha_{\mathrm{sh}} \frac{\partial f}{\partial y} \sum_{n=-N_{\mathrm{F}}}^{N_{\mathrm{F}}} \sum_{m=-N_{\mathrm{F}}}^{N_{\mathrm{F}}} \kappa_{n,m,l} \mathrm{d}\Gamma^{\mathrm{S}} \\ &- \int_{\Gamma^{\mathrm{S}}} \left(\alpha_{\mathrm{sh}} f + \beta_{\mathrm{sh}}\right) \sum_{n=-N_{\mathrm{F}}}^{N_{\mathrm{F}}} \sum_{m=-N_{\mathrm{F}}}^{N_{\mathrm{F}}} \mathrm{i}\left(n+m\right) k_{\mathrm{s}} \kappa_{n,m,l} \mathrm{d}\Gamma^{\mathrm{S}} = 0, \end{aligned} \tag{27}$$

where

$$\begin{aligned} &\alpha_{\mathrm{sh}} = \left(\frac{eC_{\mathrm{sh}}}{T_{\mathrm{e}}}\right)^3 \lambda_{\mathrm{De}}^4, \quad \beta_{\mathrm{sh}} = C_{\mathrm{th}} \lambda_{\mathrm{De}}, \\ &f = \left|\kappa\right|^3, \quad \kappa = \sum_{n=-N_{\mathrm{F}}}^{N_{\mathrm{F}}} \sum_{m=-N_{\mathrm{F}}}^{N_{\mathrm{F}}} \kappa_{n,m}, \\ &\kappa_{n,m} = \left(\varepsilon^{\mathrm{S}}_{xxn} \hat{E}^{\mathrm{S}}_{xm} + \varepsilon^{\mathrm{S}}_{xyn} \hat{E}^{\mathrm{S}}_{ym} + \varepsilon^{\mathrm{S}}_{xzn} \hat{E}^{\mathrm{S}}_{zm}\right) \mathrm{e}^{\mathrm{i}(n+m)k_{\mathrm{s}}y}, \\ &\kappa_{n,m,l} = \kappa_{n,m} \mathrm{e}^{-\mathrm{i}lk_{\mathrm{s}}y}. \end{aligned} \tag{28}$$

Here, the dielectric tensor $\boldsymbol{\epsilon}$ is expressed using a Fourier series in the same way as Eq. (20), but without multiplying it by the sheath width. The integrals in Eq. (27) are numerically evaluated by applying the three-point Gaussian quadrature rule at each divided segment on the sheath surface. Note that the number of the segments for numerical integration must be determined so as to resolve the finest Fourier harmonics (i.e., for $|n + m - l| = 3N_{\mathrm{F}}$). Due to the nonlinearity, the resultant system of discretized equations must be iteratively solved; for this purpose, we employ a Newton-Raphson method as in the previous work [11]. Although the above formulation is based on a flat sheath, the procedure can be straightforwardly generalized by decomposing the unit vector $\boldsymbol{s}$ (which is initially defined at each grid node on the boundary) in a similar way to Eq. (23) and then adding the expression into the discretized equation. As a reference, the explicit form of the finite element discretization of the sheath BC for an arbitrarily curved wall is shown in our previous paper [11].

4. Numerical analysis in 2D slab geometry

In order to assess the capability of the developed numerical scheme, we consider solutions of the 2D sheath-plasma interaction problems that were analyzed in our previous work [11, 12]. Fig. 2 shows the problem definition which corresponds to a simplified geometry of the edge plasma region including an antenna in the poloidal cross-section of a tokamak. The origin in the Cartesian coordinate system is placed at the bottom-left corner of the domain. The electric field is solved in the plasma volume Ω subject to the sheath BC on the right-hand side, the absorbing BC on the left-hand side (if necessary), and a periodic boundary condition that connects the top and bottom of the domain. The absorbing BC is an outgoing wave condition and is introduced by inserting a damping layer in the vicinity of the core-edge plasma boundary. This can be achieved by defining the electron mass as $m_{\mathrm{e}}\,(1 + \mathrm{i}\nu/\omega)$ and choosing the artificial collision frequency ν to decrease exponentially from the core-edge plasma boundary. In the geometry shown in Fig. 2, ν is described in the following equation:

$$\nu = \nu_0 \exp\left(-\frac{x}{\lambda_\nu}\right), \tag{29}$$

where ν_0 is the maximum artificial frequency, and λ_ν represents the length of the damping layer. With this procedure, the actual boundary condition

on the core side (the left-hand side in Fig. 2) is not important, so that we can impose the conducting-wall BC, $\boldsymbol{E}_\tau = \boldsymbol{0}$, for example. More details are described in Ref. [11]. The antenna surface current is given by a cosine function in the y direction as follows:

$$\boldsymbol{J}_{\text{ext}} = K(y)\,\delta(x - D_{\text{lw-ant}})\,\mathrm{e}^{\mathrm{i}(k_z z - \omega t)}\boldsymbol{e}_y, \tag{30}$$

with

$$K(y) = K_{\max}\cos^2\left(\frac{\pi\hat{y}}{L_{\text{ant}}}\right), \tag{31}$$

where $K_{\max}$ is the maximum antenna current density, and $\hat{y} = y - L_y/2$. In both linear and nonlinear problems, the global equation is computed by employing MUMPS (MUltifrontal Massively Parallel sparse direct Solver) [27] on the Hopper Cray XE6 computer system at the National Energy Research Scientific Computing Center (NERSC). The numerical results shown in this section are on the plane of $z = 0$ at $t = 2\pi l/\omega$, where l is an integer.

4.1. Code verification

4.1.1. Verification of the linear scheme

First of all, a numerical result obtained with the combined finite element and spectral method is compared with the result given by the previous numerical approach for the linear (thermal sheath) problem considered in Ref. [12]. Based on Fig. 2, the calculation domain, antenna length, and its position are determined such that $L_x = 0.6$ m, $L_y = 0.4$ m, $L_{\text{ant}} = 0.05$ m, and $D_{\text{lw-ant}} = 0.57$ m. The quasi-neutral plasma density and background magnetic field are fixed at $n_0 = 2 \times 10^{18}$ m^{-3}, $B_{0x} = 1.5$ T, $B_{0y} = 0.5$ T, and $B_{0z} = 4$ T over the whole domain. In this and subsequent analyses, the toroidal wavenumber component, k_z, is fixed at 10.8 m^{-1}, the electron temperature is 10 eV, and the applied frequency is 80 MHz. For these parameters, both fast and slow waves are evanescent away from the antenna. The calculation domain is divided by a partly uniform mesh which includes 901×961 grid points in total; 420×480 uniform nine-node elements in $0 \le x \le D_{\text{lw-ant}}$ and 30×480 uniform elements in $D_{\text{lw-ant}} \le x \le L_x$ are used in the x and y directions, respectively.

Fig. 3 shows a comparison of the real part of the parallel electric field component ($E_\parallel = \boldsymbol{E} \cdot \boldsymbol{B}_0/|\boldsymbol{B}_0|$) along the sheath surface (at $x = 0.6$ m) for $K_{\max} = 1$ A/m, in which three numerical results obtained by employing

the previous finite element method (FEM) and the combined finite element and spectral method (FESM) with $N_{\mathrm{F}} = 10$ and 30 are plotted. Here, the FEM solution corresponds to the result shown in Ref. [12]. It is seen that the FESM solution converges on the FEM solution when the cutoff number of harmonics is sufficiently large ($N_{\mathrm{F}} = 30$), although its accuracy is not enough for $N_{\mathrm{F}} = 10$. This converged solution profile represents the SPW, which was investigated through an electrostatic 2D sheath mode analysis in Ref. [12].

4.1.2. Verification of the nonlinear scheme

As a next verification, we consider solving the nonlinear self-consistent RF sheath problem, which was also analyzed in Ref. [12], by employing the proposed method. In this problem, the calculation domain, antenna length, and its position are defined such that $L_x = 0.7$ m, $L_y = 0.3$ m, $L_{\mathrm{ant}} = 0.05$ m, and $D_{\text{lw-ant}} = 0.65$ m. The plasma density is reduced to $n_0 = 1 \times 10^{17}$ m^{-3}, which is lower than the lower hybrid density and thus, a SW propagates in the cold plasma and interacts with the sheath on the material boundary. Of course, the electric field strength of the SW is enhanced as the antenna current increases. The other parameters fixed in this analysis are unchanged from the previous analysis, except that the absorbing region is inserted on the left-hand side of the domain ($\nu_0 = 3 \times 10^{11}$ s^{-1} and $\lambda_\nu = 0.05$ m); thus, it is assumed that the propagating SW is not reflected from the left boundary. The calculation domain is divided by a uniform mesh which includes 1261×781 grid points (630×390 nine-node elements in the x and y directions, respectively). For nonlinear calculations in this study, basically the same convergence criterion as described in the appendix of Ref. [11] is applied.

Fig. 4 compares the variations of the normalized normal component of the electric displacement, $|D_{\mathrm{n}}| / K_{\max}$, along the sheath surface (at $x = 0.7$ m) for $K_{\max} = 20$ and 80 A/m. Again, the FEM solutions correspond to the results shown in Ref. [12], and the FESM solutions are obtained with $N_{\mathrm{F}} = 30$. For the FESM calculations, the sheath surface is divided into 180 equally-spaced segments for numerical integration. It is confirmed that both results for the two different antenna current values are quantitatively in good agreement. Although this solution profile is not very favorable for the spectral discretization due to the presence of steep kinks, the wiggles observed here will not influence the evaluation of sputtering or power losses, etc. and thus, they do not matter for practical purposes. The normalized quantity decreases with an increase in the antenna current due to the insulating effect of the RF sheath at high sheath voltages (see Ref. [12]).

4.2. RF sheath-plasma interaction for a small contact angle

In Section 4.1, we have confirmed the validity of the proposed method by comparing the calculated results with the previously obtained finite element solutions. As a last numerical example, we consider another nonlinear case where the magnetic field lines intersect with the metal wall at a shallow angle and demonstrate stability of the new approach as compared with the previous method.

The shallow-angle case requires careful attention to the grid resolution perpendicular to the sheath surface. To demonstrate this, we conduct the analysis of an electrostatic 2D sheath mode assuming a homogeneous plasma with constant density in the equilibrium state based on the geometry shown in Fig. 2. The details of this analysis are described in Ref. [12]. Fig. 5 shows the variations of the real and imaginary parts of k_x at the sheath-plasma interface as functions of the poloidal angle of the background magnetic field for $n_0 = 1\times10^{17}$ m^{-3}. Here, the poloidal angle θ_p is defined using the poloidal components of $\boldsymbol{B}_0$ (i.e., $\tan\theta_\mathrm{p} = B_{0y}/B_{0x}$) and $\theta_\mathrm{p} = 0$ when the direction of the poloidal component vector is identical with the positive direction of the x axis. It is observed that both $|\mathrm{Re}\,(k_x)|$ and $|\mathrm{Im}\,(k_x)|$ rapidly increase at two specific angles ($\theta_\mathrm{p} = \pi/2,\ 3\pi/2$) with $|\mathrm{Im}\,(k_x)|$ larger than $|\mathrm{Re}\,(k_x)|$. This indicates that the decay length of the SPW into the plasma, which is estimated by $|\mathrm{Im}\,(k_x)|^{-1}$, gets smaller as the contact angle between the magnetic field line and the wall approaches zero and thus, fine grids are required to resolve the thin decay layer adjacent to the sheath when the magnetic field lines are close to being parallel to the wall.

With this understanding, let us first calculate a problem for a shallow contact angle using the original FEM. In this problem, the components of the background magnetic field are given by $B_{0x} = 0.5$ T, $B_{0y} = 1.5$ T, and $B_{0z} = 4$ T. In addition, the calculation domain and antenna length are adjusted to comparable sizes to the Alcator C-Mod tokamak such that $L_x = 1.5$ m, $L_y = 2.14$ m, $L_\mathrm{ant} = 0.44$ m, and $D_\mathrm{lw\text{-}ant} = 1.425$ m as in Ref. [11]. The plasma density is assumed to be spatially constant and fixed at $n_0 = 1\times10^{17}$ m^{-3}, and an absorbing layer is formed at the left boundary with $\nu_0 = 1\times10^{11}$ s^{-1} and $\lambda_\nu = 0.2$ m. For purposes of comparison, the calculation domain is divided by two different partly uniform meshes which include 801×721 and 901×721 grid points; 350×360 uniform nine-node elements in $0 \le x \le D_\mathrm{lw\text{-}ant}$ and 50, 100×360 uniform elements in $D_\mathrm{lw\text{-}ant} \le x \le L_x$ are used in the x and y directions, respectively.

Fig. 6 compares the variations of $|D_{\rm n}|/K_{\rm max}$ along the sheath surface (at $x = 1.5$ m) for $K_{\rm max} = 300$ and 400 A/m, which are obtained with two different calculation grids. First, as evidently seen, the solution for 400 grid elements in x unstably oscillates and exhibits a wrong profile in the range of $0.8 < y < 1.1$ m at $K_{\rm max} = 300$ A/m. When the grid-scale oscillation evolves like this, the Newton-Raphson iteration is hardly converged for higher antenna current values. This numerical instability is caused due to insufficient grid resolution perpendicular to the sheath surface. As evidence of this, the onset of the collapse in the FEM solution profile occurs at higher antenna current as the grid resolution in x increases in the vicinity of the sheath, which is observed in the solution profiles for 450 grid elements in x. To attain a numerical solution for $K_{\rm max} > 400$ A/m, one needs to further increase the grid resolution to resolve the decay length in the direction perpendicular to the sheath. Although this is an example for a nonlinear case, the spurious oscillations can be excited even for a linear case. However, the oscillation amplitude is much smaller compared to the largest value of $|D_{\rm n}|/K_{\rm max}$, and thus, the instability is not obvious in this case.

Next, we apply the proposed method to the same problem with the calculation domain divided by a partly uniform mesh of 801×721 grid points (see above), and the results are shown in Fig. 7. As can be seen, no numerical instability appears in the FESM solution for $K_{\rm max} = 300$ A/m, and its solution profile is correctly calculated even for a higher antenna current value, at $K_{\rm max} = 700$ A/m, showing the nonlinear insulating effect of the sheath, i.e., the reduction in $|D_{\rm n}|/K_{\rm max}$ as $K_{\rm max}$ increases. Here, the FESM solutions are obtained with $N_{\rm F} = 30$. The reason for being able to conduct a stable calculation is that the unstable oscillations of the tangential electric field components are limited to the extent where they are well resolved by the given grids, owing to the restricted number of harmonics.

When the solution involves a region where numerical instabilities are induced and the electric field strength there is expected to be small (for example, "kinks" generated as a result of the collision between a propagating SW with finite width and a wall), the proposed method can be efficiently applied to such a case by using a moderate value of $N_{\rm F}$ (which is sufficient to resolve the profile where the electric field strength is large and physically important). This feature can be useful when considering a realistic tokamak simulation, for which a significant number of calculation grids are required to resolve various important phenomena.

5. Conclusions

In this paper, we presented a combined finite element and spectral approach that solves self-consistent RF sheath-plasma interactions in a 2D domain for ICRF waves. The scheme is constructed by applying a 2D finite element method to discretize a combined form of Maxwell's equations governing the cold plasma behavior and a 1D spectral method to discretize the sheath BC at the boundary. It has been shown that the present numerical approach reproduces the previously obtained numerical results and can be stably applied to the problem in which a propagating SW interacts with a material wall at a shallow contact angle and thereby a generated SPW rapidly decays within a narrow layer adjacent to the sheath. An important feature of this method is that it prevents unstable grid-scale oscillations from expanding with increase in antenna current by introducing a cutoff in the number of harmonics in the discretization of the sheath BC.

We have been trying to obtain a physically meaningful solution with a reasonable grid resolution and a small number of harmonics; this would allow treating the entire SOL given the limited computer resources. In most cases, the important quantity in practical operation is the peak of the sheath potential, not the fine structure where the potential is small. The FESM method allows us to accurately compute the peak of the sheath potential at fixed number of harmonics without demanding the same accuracy where the sheath potential is small and relatively unimportant.

It would also be important to mention some drawbacks of the proposed method. Due to the spectral discretization of the sheath BC, the convergence of Fourier series in the tangential components of the electric field on the sheath surface depends on their solution profiles along the boundary. In some cases, a large number of harmonics could be required to reach the desired profile there. The increase in number of harmonics leads to an increase in computational time, in particular, for nonlinear cases since the RF-dominated sheath width is proportional to the cube of the normal electric displacement and the segment length for numerical integration of the discretized sheath BC needs to be shortened accordingly to capture the finest sinusoidal waves. For the above-mentioned cases, the original finite element treatment of the sheath BC can be more appropriate. Further, one always has to carefully check whether the results correctly capture any important physics, which can only be revealed with a sufficient number of calculation grids in the vicinity of (and/or along) the sheath surface. Therefore, the

present numerical approach is not intended to replace the previous finite element procedure. Instead, both techniques allow us to make a flexible choice to efficiently solve a wide variety of sheath-plasma interaction problems.

Acknowledgments

This work was supported by DOE grant No. DE-FC02-05ER54823 with Lodestar Research Corporation under the Scientific Discovery Through Advanced Computing Initiative (SciDAC). The work of H. Kohno was supported by a subcontract between Lodestar Research Corporation and Lehigh University. The research also used resources of the National Energy Research Scientific Computing Center, which is supported by the DOE under Contract No. DE-AC02-05CH11231.

Appendix A. Calculation of the coefficients $\bar{N}^{\mathrm{S}}_{m,j}$

The integral shown in Eq. (25) can be analytically calculated for the finite element interpolation N^{S}_j. Let us consider the contribution from one three-node grid element which includes the node j. The local quadratic functions N^{S}_α are defined as

$$N^{\mathrm{S}}_\alpha = \frac{\xi_\alpha \xi}{2}\left(1+\xi_\alpha \xi\right) + \left(1-\xi^2_\alpha\right)\left(1-\xi^2\right), \tag{A.1}$$

where $-1 \le \xi \le 1$, and the subscript α denotes the local node number ($\alpha = 1,2,3$); $\xi_{1,2,3} = -1,1,0$. In each grid element the y coordinate is expressed as $y = y_{\mathrm{e}} + (\Delta y/2)\,\xi$, where y_{e} is the coordinate value at the center and Δy is the length of the grid element. Thus, for $m \neq 0$ the corresponding integral is calculated as follows:

$$\int_{-1}^{1}\left(\sum_{n=0}^{2} C_n \xi^n\right) \mathrm{e}^{a\xi+b}\mathrm{d}\xi = \sum_{n=0}^{2} C_n F\left(n\right), \tag{A.2}$$

where

$$F\left(n\right) = \begin{cases} \left[\frac{\xi^n}{a}\mathrm{e}^{a\xi+b}\right]_{-1}^{1} - \frac{n}{a}F\left(n-1\right) & \text{for } n \ge 1 \\ \frac{1}{a}\left(\mathrm{e}^{a+b} - \mathrm{e}^{-a+b}\right) & \text{for } n = 0, \end{cases} \tag{A.3}$$

with

$$
\begin{aligned}
&C_0 = 1 - \xi_\alpha^2, \quad C_1 = \frac{\xi_\alpha}{2}, \quad C_2 = \frac{3}{2}\xi_\alpha^2 - 1, \\
&a = -\mathrm{i}mk_\mathrm{s}\frac{\Delta y}{2}, \quad b = -\mathrm{i}mk_\mathrm{s}y_\mathrm{e}.
\end{aligned}
\tag{A.4}
$$

For $m = 0$, Eq. (A.2) reduces to

$$
\int_{-1}^{1} \sum_{n=0}^{2} C_n \xi^n \mathrm{d}\xi = 2\left(C_0 + \frac{C_2}{3}\right). \tag{A.5}
$$

Consequently, the coefficient $\bar{N}^\mathrm{S}_{m,j}$ for each value of m at fixed j is calculated by summing the local integrals (or one local integral for $\alpha = 3$) that include(s) nonzero part of the shape function N^S_j.

References

[1] Freidberg JP. Plasma physics and fusion energy. Cambridge University Press; 2007.

[2] Wesson J. Tokamaks (third edition). Oxford University Press; 2004.

[3] Stix TH. Waves in plasmas. American Institute of Physics; 1992.

[4] D'Ippolito DA, Myra JR, Bureš M, Jacquinot J. A model of sheath-driven impurity production by ICRF antennas. Plasma Phys. Control. Fusion 1991; 33: 607–642.

[5] Bureš M, Jacquinot J, Lawson K, Stamp M, Summers HP, D'Ippolito DA, Myra JR. Impurity release from the ICRF antenna screens in JET. Plasma Phys. Control. Fusion 1991; 33: 937–967.

[6] Noterdaeme JM, Van Oost G. The interaction between waves in the ion cyclotron range of frequencies and the plasma boundary. Plasma Phys. Control. Fusion 1993; 35: 1481–1511.

[7] Lipschultz B, Pappas DA, LaBombard B, Rice JE, Smith D, Wukitch SJ. A study of molybdenum influxes and transport in Alcator C-Mod. Nucl. Fusion 2001; 41: 585–596.

[8] Hosea J, Bell RE, LeBlanc BP, Phillips CK, Taylor G, Valeo E, Wilson JR, Jaeger EF, Ryan PM, Wilgen J, Yuh H, Levinton F, Sabbagh S, Tritz K, Parker J, Bonoli PT, Harvey R, NSTX Team. High harmonic fast wave heating efficiency enhancement and current drive at longer wavelength on the National Spherical Torus Experiment. Phys. Plasmas 2008; 15: 056104.

[9] Myra JR, D'Ippolito DA, Russell DA, Berry LA, Jaeger EF, Carter MD. Nonlinear ICRF-plasma interactions. Nucl. Fusion 2006; 46: S455–S468.

[10] D'Ippolito DA, Myra JR. ICRF-edge and surface interactions. J. Nucl. Mater. 2011; 415: S1001–S1004.

[11] Kohno H, Myra JR, D'Ippolito DA. A finite element procedure for radio-frequency sheath-plasma interactions in the ion cyclotron range of frequencies. Comput. Phys. Commun. 2012; 183: 2116–2127.

[12] Kohno H, Myra JR, D'Ippolito DA. Numerical analysis of radio-frequency sheath-plasma interactions in the ion cyclotron range of frequencies. Phys. Plasmas 2012; 19: 012508.

[13] Myra JR, D'Ippolito DA, Bures M. Far field sheaths from waves in the ion cyclotron range of frequencies. Phys. Plasmas 1994; 1: 2890–2900.

[14] D'Ippolito DA, Myra JR. A radio-frequency sheath boundary condition and its effect on slow wave propagation. Phys. Plasmas 2006; 13: 102508.

[15] Gottlieb D, Orszag SA. Numerical analysis of spectral methods: theory and applications. Society for Industrial and Applied Mathematics; 1977.

[16] Canuto C, Hussaini MY, Quarteroni A, Zang TA. Spectral methods in fluid dynamics. Springer-Verlag; 1987.

[17] Fornberg B. A practical guide to pseudospectral methods. Cambridge University Press; 1996.

[18] Brambilla M, Krücken T. Numerical simulation of ion cyclotron heating of hot tokamak plasmas. Nucl. Fusion 1988; 28: 1813–1833.

[19] Bernardi C, Debit N, Maday Y. Coupling finite element and spectral methods: first results. Math. Comput. 1990; 54: 21–39.

[20] Guo BY, Cao WM. A combined spectral-finite element method for solving two-dimensional unsteady Navier-Stokes equations. J. Comput. Phys. 1992; 101: 375–385.

[21] Tahani A, Salon S, Chari MVK. Coupled finite element and Fourier transform method for transient scalar field problems. Elec. Mach. Power Syst. 1996; 24: 65–81.

[22] Meddahi S, Márquez A. A combination of spectral and finite elements for an exterior problem in the plane. Appl. Numer. Math. 2002; 43: 275–295.

[23] Child CD. Discharge from hot CaO. Phys. Rev. (Series I) 1911; 32: 492–511.

[24] Langmuir I. The effect of space charge and initial velocities on the potential distribution and thermionic current between parallel plane electrodes. Phys. Rev. 1923; 21: 419–435.

[25] Lieberman MA. Analytical solution for capacitive RF sheath. IEEE Trans. Plasma Sci. 1988; 16: 638–644.

[26] Godyak VA, Sternberg N. Dynamic model of the electrode sheaths in symmetrically driven rf discharges. Phys. Rev. A 1990; 42: 2299–2312.

[27] Amestoy PR, Duff IS, L'Excellent JY. Multifrontal parallel distributed symmetric and unsymmetric solvers. Comput. Methods in Appl. Mech. Eng. 2000; 184: 501–520. (Also, see the following website: http://mumps.enseeiht.fr/)

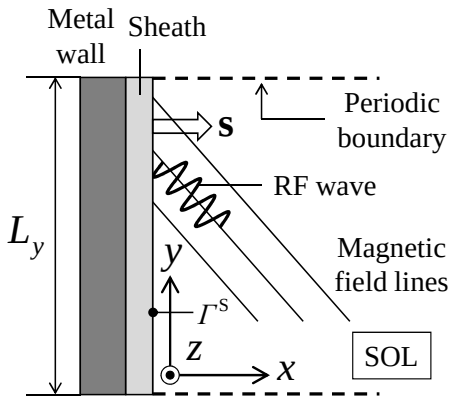

Figure 1: Model geometry for the spectral discretization of the sheath BC.

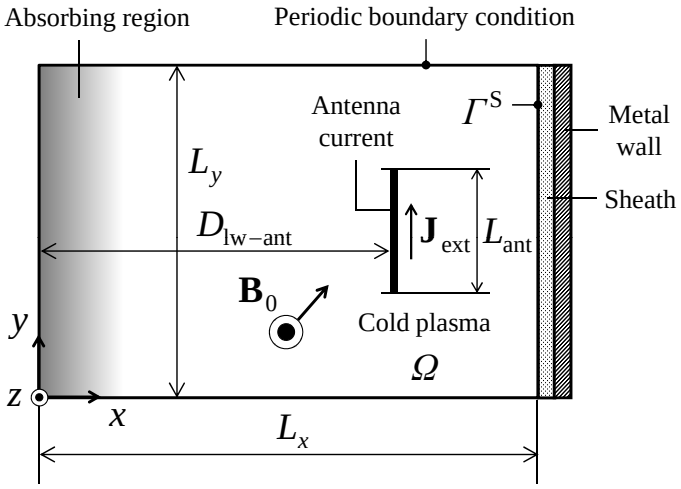

Figure 2: Singly periodic slab model to analyze RF sheath-plasma interactions.

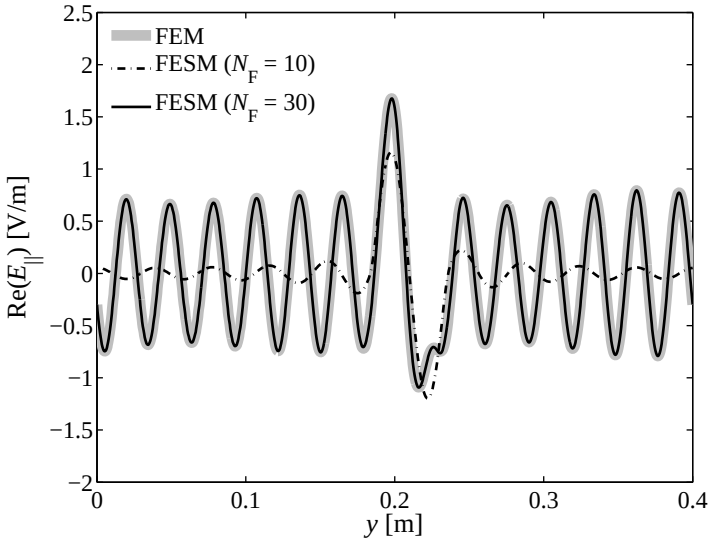

Figure 3: Comparison of the real part of the parallel electric field component on the thermal sheath between the two different numerical methods.

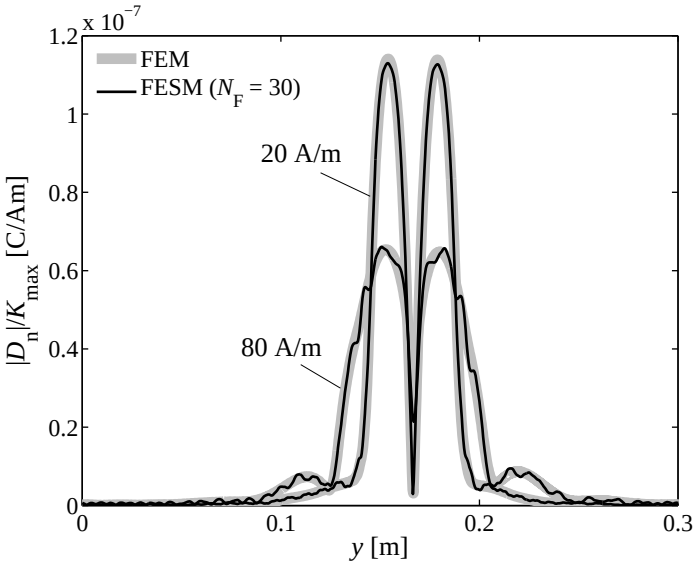

Figure 4: Comparison of the normalized normal component of the electric displacement on the RF sheath between the two different numerical methods for a large contact angle of the magnetic field line on the sheath surface ($\sin\vartheta = 0.35$).

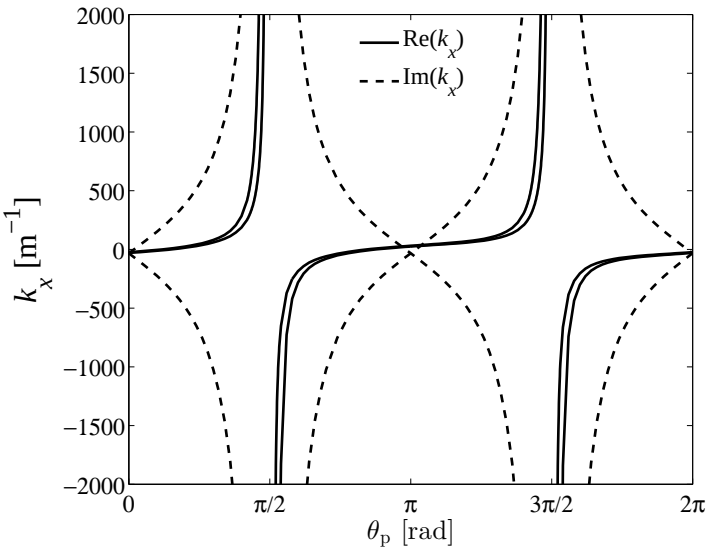

Figure 5: Plot of the real and imaginary parts of k_x at the sheath-plasma interface as functions of the poloidal angle of the background magnetic field for $n_0 = 1 \times 10^{17}$ m^{-3}. The angles of $\theta_p = \pi/2$, $3\pi/2$ are when the background magnetic field is tangent to the sheath surface.

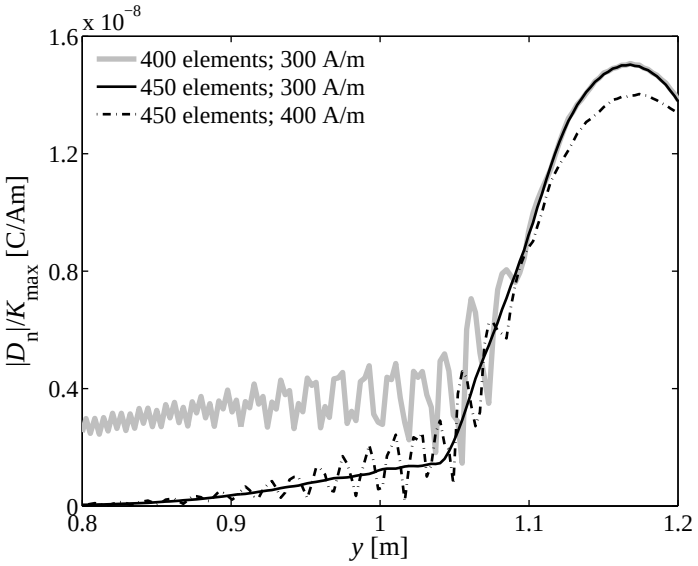

Figure 6: Comparison of the normalized normal component of the electric displacement obtained by applying the original FEM on two different calculation grids to the analysis for a small contact angle of the magnetic field line on the sheath surface. The number of elements denotes the number of total grid elements in the x direction.

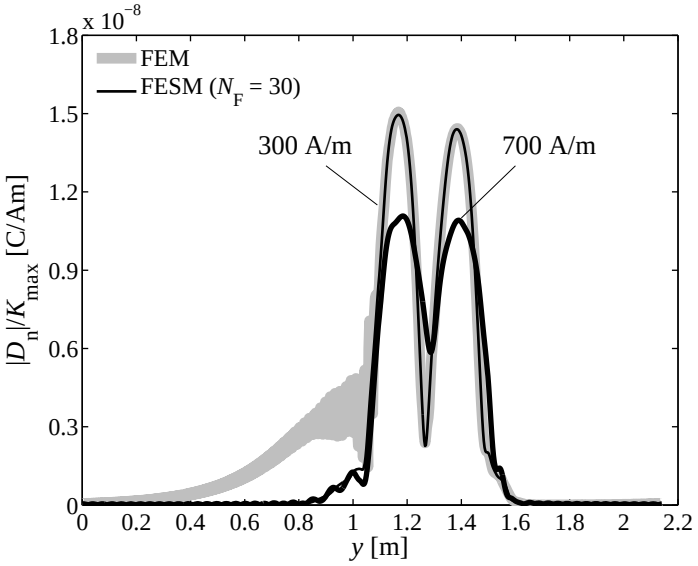

Figure 7: Comparison of the normalized normal component of the electric displacement on the RF sheath between the two different numerical methods for a small contact angle of the magnetic field line on the sheath surface ($\sin\vartheta = 0.12$).